JOURNAL OF AIRCRAFT
Vol. 42, No. 6, November–December 2005

Approach to Induced Drag Reduction with Experimental Evaluation

David Eller* and Sebastian Heinze†
Royal Institute of Technology, SE-100 44 Stockholm, Sweden

An approach to minimize the induced drag of an aeroelastic configuration by means of multiple leading- and trailing-edge control surfaces is investigated. A computational model based on a boundary-element method is constructed and drag-reducing flap settings are found by means of numerical optimization. Further, experiments with an elastic wind-tunnel model are performed in order to evaluate the numerically obtained results. Induced-drag results are obtained by analyzing lift distributions computed from optically measured local angles of attack because standard techniques proved insufficient. Results show that significant reductions of induced drag of flexible wings can be achieved by using optimal control surface settings.

Introduction

OPTIMIZATION of aerodynamic drag is commonly concerned with finding the optimal shape of a body with minimal drag for a specified, fixed flight condition. Because the aircraft shape is not usually assumed to be variable in operation, some sort of compromise has to be found for vehicles that need to operate efficiently within a wide range of lift coefficients, Mach numbers, or altitudes. Examples of such aircraft can be 1) commercial transports with extremely long range, where the aircraft weight changes considerably during cruise caused by fuel consumption; 2) long-range unmanned aerial vehicels with a possibly even higher fuel weight fraction; or 3) vehicles with wide operating envelopes that might need to operate and maneuver at widely varying speeds and altitudes. In such cases, a system that could minimize induced drag within most or all of the operational envelope would be beneficial. Clearly, optimization of the external shape alone cannot provide optimal performance for a wide range of operational parameters, especially when considering aeroelastic deformations.[1]

Another aspect of induced drag minimization is that maneuver performance can be considerably improved for some vehicles. Lightweight long-range aircraft tend to have rather limited excess power to overcome the additional induced drag incurred by the increased lift necessary for maneuvering.[2] Means to adaptively provide a wing configuration with minimum induced drag for maneuvering conditions could therefore improve operational flexibility.

To obtain efficient baseline performance, vehicles of the type just mentioned will likely feature lightweight high-aspect-ratio wings leading to considerable flexibility and corresponding aeroelastic deformations even in cruise flight. Because the influence of this deformation on the spanwise lift distribution can be very considerable, it needs to be included in an analysis of induced drag. In this context, "induced drag" refers to the drag caused by the spanwise distribution of lift and does not include other drag components that might also depend on lift to some degree.

The most straightforward method to enable drag optimization under different flight conditions is the provision of a certain number of conventional control surfaces at the leading and trailing edges of the lifting surfaces.[1] Variable camber wings or controllable wing-tip extensions are interesting alternative concepts that might require more system integration efforts.[3,4] Flap-based active aeroelastic control has been investigated[5,6] and successfully evaluated experimentally for maneuverability improvements and load alleviation, although usually with a fixed set of control surfaces.[3,7] Kuzmina et al.[8] presented a numerical study showing the possibility of reducing induced drag of elastic aircraft using control surfaces.

The aim of this study is to investigate which and how many control surfaces are required to achieve a worthwhile reduction in induced drag for a highly flexible lifting surface. In particular, the optimal configurations determined numerically are to be tested in the wind tunnel in order to evaluate if the computed drag reductions can be obtained. Experimental determination of induced drag requires a method to separate the induced-drag component from the measured total drag.

Because induced drag constitutes only a certain fraction of the overall aircraft drag, employing an optimal setup of deflected control surfaces might or might not reduce total drag. Possible sources of additional viscous drag could be premature transition triggered by upstream control surfaces or flow separation caused by the disturbance of the chordwise pressure distribution. However, even airfoils for low-Reynolds-number flow can be designed for extremely low profile drag at trailing-edge flap deflections of up to 15 deg (e.g., see Althaus[9]). It should hence be possible to achieve reasonable values of viscous drag coefficients at least within a range of moderate control surface deflections.

Test Case

Within the framework of the European Union project Active Aeroelastic Aircraft Structures (3AS, Schweiger and Suleman[10]), a wind-tunnel model has been designed and built for aeroservoelastic investigations. The 1.6-m semispan model consists of a load-carrying beam of carbon-fiber composite and 10 aerodynamic sections rigidly clamped to the beam in a manner that prevents them from contributing stiffness to the beam structure. The beam can easily be replaced to allow for modification of the stiffness properties. Each segment is fitted with leading- and trailing-edge flaps, controlled by two miniature electric actuation devices driving an internal geared transmission for high deflection angle accuracy.

The airfoil used in a related full-scale design study, with 16% thickness and 3.6% camber, is also used for the model sections. Designed for velocities above Mach 0.5 and Reynolds numbers in the range of 10^7, this wing is not expected to perform optimally in terms of profile drag under low-speed wind-tunnel testing conditions with Reynolds numbers of about 3×10^5. To avoid excessive profile drag, flap deflections are therefore limited to moderate angles of ± 10 deg. With a corresponding full-span aspect ratio Λ of 20 and 10 deg wing sweep, the wing model is considered to be a reasonable

---

Presented as Paper 2004-1513 at the AIAA/ASME/ASCE/AHS/ASC 45th Structures, Structural Dynamics and Materials Conference, Palm Springs, CA, 19–22 April 2004; received 6 July 2004; revision received 15 March 2005; accepted for publication 31 March 2005.

*Ph.D. Student, Division of Flight Dynamics, Teknikringen 8; dlr@kth.se.

†Ph.D. Student, Division of Flight Dynamics, Teknikringen 8; sepp@kth.se.

Table 1 Stiffness distribution along the span

Section	1–4	5–6	7–8	9–10
EI, Nm^2	437.8	299.6	156.7	31.1
GJ, Nm^2	35.7	23.5	11.7	5.7

Table 2 Vibration testing results

Mode	f_{exp}, Hz	f_{pred}, Hz	Error, %
First bend	3.2	3.14	−1.9
First in-plane	6.0	6.06	1.0
Second bend	14.8	14.5	−2.0
First tor	17.4	17.0	−2.3
Second in-plane	32.9	32.3	−1.8
Third bend	33.6	32.8	−2.4
Second tor	39.0	39.8	2.0
Fourth bend	54.1	56.8	4.9
Third in-plane	82.6	78.3	−5.3

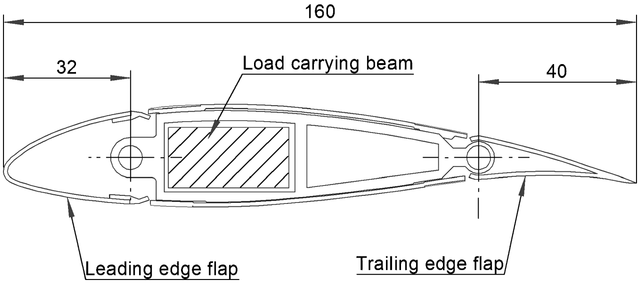

Fig. 1 Sectional view of the wind-tunnel model sections.

approximation of the generic high-altitude long-endurance unmanned aerial vehicle under investigation by 3AS project partners.

A section of the wind-tunnel model showing the arrangement of the structural beam and the control surfaces is shown in Fig. 1. Leading-edge flaps have a depth of 20% chord, those at the trailing edge 25%. The spanwise slots between the rigid shell and the control surfaces are sealed using elastic polymer strips, which are used for the same purpose on high-performance gliders.

The elastic axis is located at 36% chord, in the center of the load-carrying beam. The structural properties of the beam vary along the span of the wing. There are four regions where the beam thickness and thus stiffness is kept constant. The first region with the highest stiffness covers four inboard sections. The remaining regions are covering two sections each, with decreasing beam thickness as the span coordinate increases. The laminate is free of membrane-bending coupling. Stiffness values are shown in Table 1.

Numerical Modeling

Instead of a full-scale wing, the wind-tunnel model itself was modeled for the numerical optimization process in order to simplify comparison with experimental data. In the following, the modeling approach used to obtain the objective function and constraints for the optimization problem is described.

Structure

The structural model used for numerical simulations was validated experimentally. The preliminary stiffness distribution that was derived from composite material properties and static experiments was updated by matching experiments with static loading and measured eigenfrequencies. A comparison of predicted and measured eigenfrequencies is shown in Table 2. Especially in the lower-frequency range, the measured data fits very well with the predictions. Mass properties were not updated when matching the model to the vibration testing data because the mass distribution could be determined analytically with high accuracy.

Experiments showed furthermore that the flexibility of the wind-tunnel mounting about the x axis had to be included in order to correctly model the structural behavior. From experimental measurements, the relevant rotational stiffness around the x axis was found as 1950 Nm/rad. In the finite element model, the mounting was included as a torsional spring between wing root and wind-tunnel wall.

Aerodynamics

An unstructured boundary-element method is used to compute the aerodynamic loads for the elastic wind-tunnel model. Whereas the method employs an approach generally similar to conventional three-dimensional panel methods, it allows for simulations with moving and deforming meshes and features a variant of the Kutta condition suitable for configurations with rotating control surfaces. Aerodynamic forces and moments are obtained from surface-pressure integration. Some details on the boundary-element method are given next; more information can be found in Eller and Carlsson.[11]

Flow Model

The method solves the linearized equations of potential flow. The wetted surface of the body is discretized, and a piecewise linear distribution of source and doublet potentials is assumed on the surface. The boundary condition of flow parallel to the surface can be written as a Dirichlet condition for the potential at each collocation point, which leads to a system of linear equations. Although the general approach differs little from the conventional panel methods described in Katz and Plotkin,[12] the numerical solution makes use of panel clustering[13] in order to improve the algorithmic scaling properties. By employing a preconditioned iterative linear solver, very large problems can be solved with moderate computational cost. The method differs from the doublet lattice method[14] often used in aeroelasticity in that the true surface shape including wing thickness is geometrically modelled. It is hoped that the higher geometric fidelity improves the prediction of control surface effects. Boundary-layer displacement, however, is not accounted for yet.

Discretization

Unstructured triangular surface meshes are used in order to allow the treatment of complex geometries. Because the geometry of the wind-tunnel model considered here is rather simple, triangulated structured meshes are used to reduce the number of surface elements. Control surface motion is modeled by rotating appropriate subsets of the surface mesh around the corresponding hinge axis. The gaps that would normally open to the left and right of the moving surface elements are not modeled; instead, some surface elements are stretched to cover the gaps. This approach yields satisfactory meshes for flap deflection up to at least 15 deg without special mesh refinement, which is more than sufficient for the current study. In Fig. 2, the overall geometry of the surface used in the simulation is shown, together with a detailed view of the mesh in the vicinity of a deflected control surface. Symmetric flow is enforced by modeling the half-wings on both sides of the symmetry plane.

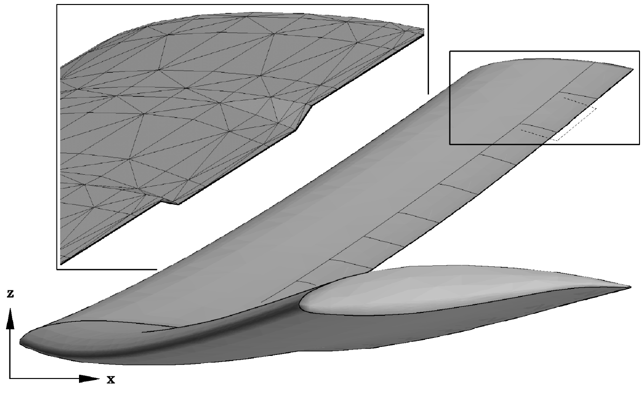

Fig. 2 Shape of the complete deformed wing. Insert shows coarse mesh of the wing-tip region with the ninth trailing-edge flap deflected 10 deg down.

Kutta Condition

As the solution of the governing equation of steady potential flow alone cannot yield a resulting force on a closed body, a wake surface carrying doublet singularities must be modeled. The strength of these doublets is determined by introducing additional equations that enforce the Kutta condition for the resulting flowfield. However, because the Kutta condition is empirical, different mathematical formulations exist. When the condition is enforced in terms of a vanishing vortex strength along the trailing edge,[12] or as a function of flow velocity components normal to the surface, large velocity gradients can result when the trailing edge is not smooth along the span. Alternatively, the Kutta condition can be expressed in terms of tangential velocity components. As the surface tangent vectors in the downstream direction do not change as radically as the surface normals in the flap region, smooth pressure distributions are obtained.

Force Integration

Some difficulty is introduced by the relatively poor "conditioning" of the drag computation by pressure integration. Because the drag force is a fairly small component of the resulting aerodynamic forces acting on the wing, and thus a small difference of fairly large pressure forces acting in different directions, small relative errors in surface pressures can lead to significantly larger relative drag errors. For the coarsest mesh used in this study, with about 4000 surface elements, the absolute error in induced drag coefficient was found to be approximately 0.003 when compared with measurements. In general, this is a fairly good accuracy when compared to drag coefficients for complete configurations. Unfortunately, for a very high-aspect-ratio wing, this error constitutes a sizeable fraction of the induced drag at low lift coefficients.

Boundary-Layer Effects

As mentioned before, wind-tunnel testing was restricted to rather low Reynolds numbers in the order of 3×10^5. For such conditions, viscous effects play an important role. For example, laminar separation bubbles are relatively likely to occur.[15] Although this study is not concerned with the associated increase in profile drag, even small separations can lead to a pressure distribution that differs somewhat from the inviscid one computed by the numerical method. Furthermore, turbulent boundary layers grow rather quickly at low Reynolds numbers and can reach a thickness of several percent chord at the trailing edge. Lacking symmetry between upper and lower airfoil side, such thick boundary layers usually reduce the effective camber of the wing, changing both lift and section pitch moment.

Naturally, these issues affect the comparison of experimental and computed results negatively. In earlier work,[11] with Reynolds numbers exceeding 10^6, considerably better agreement could be obtained. Nevertheless, the current method achieves sufficient accuracy in predicting the spanwise distribution of loads and deformations for a given total lift, so that the induced drag optimization can be performed. At Reynolds numbers more typical for full-scale applications, boundary-layer thicknesses tend to grow more slowly, and separation bubbles are less likely, so that better agreement would be expected.

Aeroelastic Coupling

For the structural model, a simple beam approximation was chosen because the actual load carrying structure is long and slender. A Nastran[16] finite element model was constructed for the internal wing beam. From this, a reduced stiffness matrix K could be obtained for the set of 10 locations where the rigid aerodynamic sections are attached. Pressure values from the aerodynamic analysis are integrated to obtain forces and moments for each of the wind tunnel model sections. These loads are applied as point loads acting on the section attachments, from which beam deformations are computed. Beam deformations u can then be mapped to surface vertex displacements using an interpolation procedure.

To solve the static aeroelastic problem

$$Ku = F_a(u, \delta) \tag{1}$$

where F_a contains the aerodynamic loads on the model segments, depending on the beam displacements u and the vector of control surface deflections δ, a damped fixed-point iteration is employed:

$$u^{k+1} = (1 - \omega)u^k + \omega K^{-1} F_a(u^k, \delta) \tag{2}$$

With a damping factor $\omega = 0.7$, the simple iteration method converges within four to six steps, which makes it computationally efficient. As the condition for convergence, the relative change of the surface doublet strengths between consecutive iterations was required to fall below 1%,

$$|\boldsymbol{\mu}^k - \boldsymbol{\mu}^{k-1}| < 0.01|\boldsymbol{\mu}^k| \tag{3}$$

where $\boldsymbol{\mu}^k$ is the vector of doublet strengths at step k. A similar criterion can be defined for the deformations u, but Eq. (3) was found to be somewhat more strict because doublet strengths converged at a slower rate than deformations.

Problem (1) can also be treated by computing the Jacobian

$$J = K - \frac{\partial F_a}{\partial u} \tag{4}$$

and applying Newton's method. Because, for small deformations u, aerodynamic loads are almost linearly dependent on u, a single step is often sufficient. For linear aeroelastic stability problems, where infinitesimally small deformations are considered, this approach is accurate and efficient. With the current boundary-element method however, the computation of J is much more costly than a few iterations of Eq. (2), which only take a few seconds each. For high airspeeds close to static aeroelastic divergence, J becomes nearly singular, and the rate of convergence for a simple method as Eq. (2) would degrade rapidly. In that case, a direct solution (or Newton's method for large deformations) is usually more efficient.

To evaluate if the simplified aerodynamic model is sufficiently accurate, numerical results for static equilibrium deformations are compared with measured data in Fig. 3. The optical measurement system tracks marker positions only, so that twist values given in Fig. 3 are computed from differences of marker displacements and hence are less accurate than translational deflections. Tip deflections are relatively large, reaching 7.5% of the semispan and about 4 deg at the wing tip for $C_L = 0.5$ at 30 m/s.

The coarse mesh with 4020 surface elements matches the measured twist deformation well and overpredicts bending deflections only marginally. The finer meshes with 7060 and 11,220 elements, respectively, are slightly closer to the measured bending deflections, but overpredict twist instead. From earlier studies, it is known that normal forces converge rather quickly with mesh refinement, while

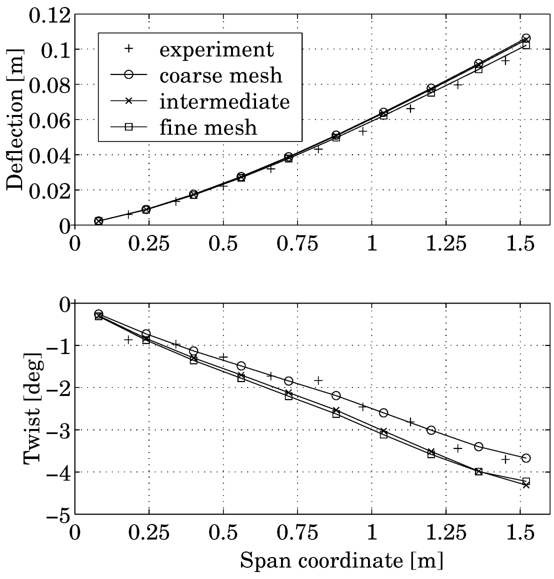

Fig. 3 Comparison of static aeroelastic deformation.

section pitch moments require slightly higher mesh resolution for good accuracy. Therefore, it must be concluded that the finer meshes represent more accurate solutions of the linear potential flow model, but that the actual twist moments encountered in the wind tunnel are smaller than the flow model predicts.

The optimization described later is performed with the coarse mesh because, in this particular case, it actually predicts twist deformations better than a numerically more accurate solution of the potential flow equations.

Optimization

Two different formulations of the drag-minimization problem were tested in this study. Although both approaches were tested, results are presented only for the second alternative, which proved superior for the problem considered. In the first approach, the drag minimization was formulated as a straightforward nonlinear programming problem of the form

Minimize:

$$C_{\mathrm{Di}}(\boldsymbol{\delta}) \tag{5}$$

Subject to:

$$C_L \geq C_{\mathrm{L,ref}} \tag{6}$$

and

$$\delta_l \leq \boldsymbol{\delta} \leq \delta_u \tag{7}$$

where C_{Di} is the coefficient of induced drag, C_L the lift coefficient constrained to be larger than some reference value $C_{\mathrm{L,ref}}$, and $\boldsymbol{\delta}$ the vector of n_d design variables holding the deflection angles of the control surfaces, bounded by the lower and upper limit angles δ_l and δ_u. The drag coefficient C_{Di} is in this case computed by pressure integration.

Because the lift coefficient depends approximately linearly on flap deflections for the range of deflection angles considered, the lift constraint (6) can be expressed as a linear inequality

$$\nabla_\delta C_L \cdot \delta \geq C_{\mathrm{L,ref}} - C_L|_{\delta=0} \tag{8}$$

with the vector of control surface derivatives $\nabla_\delta C_L$. Formulating the lift constraint in a linear manner leads to reduced computational cost in the optimization process.

The nonlinear programming problem (5–7) was solved approximately using the quasi-Newton method built into MATLAB,[17] which evaluated the objective function between 40 and 500 times, depending on the number of design variables. Solutions obtained in this way yield flap settings that reduced the computed induced drag. The weak point of this approach was found to be the drag computation by pressure integration, which required a very fine mesh for accurate results. With moderate resolution like that used to test this optimization approach, the gradients $\nabla_\delta C_{\mathrm{Di}}$ computed by the optimization software in each iteration were not sufficiently accurate, so that the quasi-Newton iteration converged toward points which were not really optimal. With better mesh resolution, computational costs became unacceptable because of the large number of function evaluations.

In contrast to induced drag, normal forces can be computed with reasonable accuracy even with rather coarse meshes. To allow for a more efficient formulation of the optimization problem, the computed spanwise distribution of circulation Γ is compared with an elliptic distribution Γ_e, which is known to be optimal for a subsonic wing-only configuration. Instead of a nonlinear programming problem, a least-squares problem of the form

Minimize:

$$|\Gamma(\boldsymbol{\delta}, y_i) - \Gamma_e(y_i)|^2 \tag{9}$$

Subject to:

$$\delta_l \leq \boldsymbol{\delta} \leq \delta_u \tag{10}$$

is obtained. Here, the lift distribution is expressed in terms of the distribution of circulation strengths $\Gamma(\delta, y_i)$ at a number of span coordinates y_i. Because of the approximate linearity of the lift distribution with respect to flap deflections, the least-squares problem can efficiently be solved in its linear form, where

$$\Gamma(\boldsymbol{\delta}, y) \approx \Gamma_0(y) + \nabla_\delta \Gamma \boldsymbol{\delta} \tag{11}$$

In this case, only the circulation distribution $\Gamma_0(y)$ for a reference case and the Jacobian $\nabla_\delta \Gamma$ with respect to flap deflections need to be computed. The reference case would usually be the configuration with neutral flap settings, where the required lift coefficient is achieved by setting an incidence angle at the wing root. Lift constraints are not necessary in this formulation because an optimal solution approximates the elliptic distribution with the correct total lift as closely as possible. This approach resembles the drag minimization procedure of Kuzmina et al.[8] in that it uses the circulation distribution. The difference is that, here, the induced drag is not computed from Γ within the optimization. Instead, the circulation distribution is used to form a more readily solved least-squares problem, which is possible in the present case.

When formulating the problem according to Eqs. (9) and (10), a relatively coarse mesh will suffice as only the lift distribution is needed, not the integrated drag value. Furthermore, computing the Jacobian by finite differences is possible using only $n_d + 1$ solutions of the static aeroelastic problem, as opposed to the $n_d + 1$ solutions required to compute the gradient in *each iteration* of a nonlinear optimization solver, where n_d is the number of design variables.

The number of design variables can be varied while the physical model with its 20 control surfaces per semispan is left unchanged, simply by deflecting groups of control surfaces together. With 10 design variables, pairs of flaps (two leading-edge or two trailing-edge surfaces) are deflected to identical positions, whereas with four variables, outboard groups of four and inboard groups of six surfaces are moved to the same deflection. Figure 4 shows a sketch of the configurations investigated. Note that, in the case with $n = 3$, only trailing-edge surfaces are deflected, but the pattern of flap deflections (4-4-2 surfaces operated in groups) is identical to the case with six variables. The angle of attack at the wing root α is an additional design variable because a change in α induces different changes in spanwise lift and moment distribution than flap deflections. However, it is likely that the parasitic drag of the fuselage and other nonlifting aircraft components would increase strongly should the angle of attack deviate substantially from some optimal range. Therefore, α is constrained to lie between the somewhat arbitrary bounds −2 and 4 deg.

In some cases, optimization resulted in flap settings featuring large differences in deflection for neighboring control surfaces. It is likely that such a configuration would increase viscous drag substantially. Therefore, additional constraints were introduced in Eqs. (9) and (10) in order to avoid large differences in deflections. For each pair of neighboring flaps $(i, i+1)$, two conditions of the form

$$\delta_i - \delta_{i+1} \leq 4\,\mathrm{deg} \tag{12}$$

$$\delta_{i+1} - \delta_i \leq 4\,\mathrm{deg} \tag{13}$$

are imposed. The limit 4 deg was chosen rather arbitrarily and was intended to be conservative in order to evaluate the impact of this

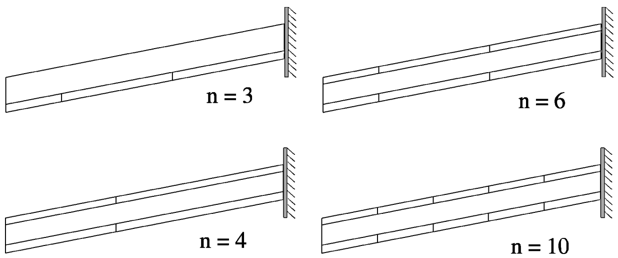

Fig. 4 Control surface configurations.

type of constraint on the optimal result. However, the optimal induced drag increased only marginally when the preceding constraint was enforced, whereas the optimal flap settings did change considerably. Small variations of the optimal value in spite of considerable differences in flap deflections indicate that a certain optimal lift distribution can be approximated closely by more than one unique flap deflection pattern.

Wind-Tunnel Experiments

Wind-tunnel experiments were performed in the low-speed wind tunnel L2000 at Royal Institute of Technology (KTH). The tunnel has a 2 × 2 m cross section with corner fillets and was operated at room temperature and atmospheric pressure. The wing was mounted vertically on the wind-tunnel floor. For some experiments, the flexible internal wing structure was replaced by a comparably stiff solid steel beam to investigate flap efficiencies and viscous effects.

Aerodynamic loads were measured using a six degree-of-freedom internal balance mounted in the wing root. A splitter plate was placed between the wing and the balance to reduce boundary-layer interactions with the wind-tunnel floor. The elastic deformation of the wing was captured using an optical measurement system[18,19] based on four charge-coupled device (CCD) cameras. Each of the cameras emits infrared flashes and monitors the two-dimensional position of passive reflecting markers attached to the model. By combining the pictures, the three-dimensional position of the markers results from the relative position of the cameras. A sketch of the experimental setup is shown in Fig. 5.

Viscous Drag

Because total drag values from the balance measurements appeared to be higher than the expected drag, an investigation of the impact of the low Reynolds number was performed. For this, the wing was equipped with the rigid beam structure and aerodynamic coefficients were measured at increasing dynamic pressure. The total drag was found to be significantly higher for low Reynolds numbers. When increasing the Reynolds number from 1.5×10^5 to 3.5×10^5, the measured drag coefficient was reduced by almost 50%. The reason for this might be a fairly thick boundary layer at low airspeeds and possibly regions of laminar flow separation. Because of experimental limitations such as flutter speed and maximum balance loading, testing with the flexible beam was restricted to airspeeds below 30 m/s, corresponding to a Reynolds number of about 3×10^5. This explains the comparatively high total drag values measured during drag-optimization investigations.

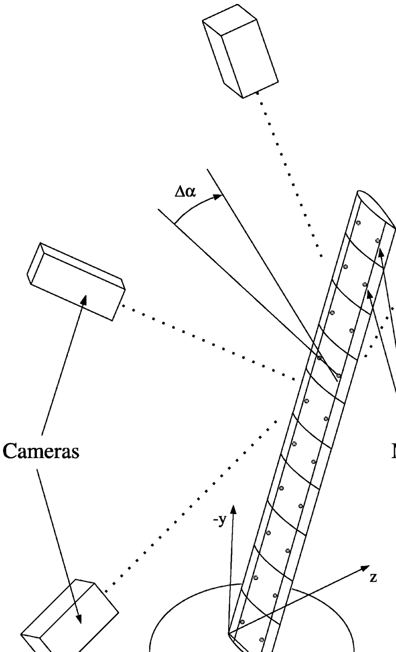

Fig. 5 Optical deformation measurement using the QualiSys infrared camera system.

Induced Drag Extraction

To compare experimental measurements with the numerical analysis performed, the induced drag had to be extracted from the measured total drag. Because of viscous effects, however, approaches as described in Barlow et al.[20] based on the measured wing-root loads turned out to be insufficient. Therefore, lifting-line theory[21] was employed for deriving the induced drag from wing deformation measurements. Because both the two-dimensional lift-curve slope $c_{l,\alpha,2d}$ and the corresponding sectional zero-lift angle α_0 are variables in the lifting-line formulation, it can be adapted to reproduce the behavior of the wind-tunnel model, for which $c_{l,\alpha,2d} = 5.33$ and $\alpha_0 = -3.1$ deg were obtained from experiments with the rigid beam structure. With these modifications, the lifting-line method accounts for boundary-layer effects that lead to a reduction of three-dimensional lift in comparison to the case of inviscid flow.

The geometric angles of attack according to

$$\alpha_g(y) = \alpha - \alpha_0 + \Delta\alpha(y) + \frac{\partial \alpha}{\partial \delta_T}\delta_T(y) + \frac{\partial \alpha}{\partial \delta_L}\delta_L(y) \tag{14}$$

served as input to the lifting-line computations, where α is the angle of attack of the wing root, α_0 is the measured zero-lift angle of attack of the rigid wing, and $\Delta\alpha(y)$ is the local twist deformation measured by the optical system (Fig. 5). Deflections of leading-edge δ_L and trailing-edge flaps δ_T were accounted for by adjusting the local angle of attack accordingly. The flap efficiencies

$$\frac{\partial \alpha}{\partial \delta} = \frac{\partial \alpha}{\partial C_L} \cdot \frac{\partial C_L}{\partial \delta} \tag{15}$$

were obtained from experiments with the rigid beam.

With the distribution of local angles of attack, the spanwise distribution of circulation strengths and downwash angles is then calculated using Multhopp's method[22] with 511 support points. Using the circulation strengths and downwash angles at the support points, lift and induced drag coefficients are obtained. Experimental values for the induced drag given in the following are all computed from spanwise twist deformations using this approach. Strictly speaking, the lifting-line method is only valid for plane, unswept wings as it does not account for spanwise flow. For the small sweep angle of the current wing, it is still considered a valid approximation.

Experimental Accuracy

The accuracy of the experimental results was estimated based on uncertainties of measured variables. Confidence intervals were calculated for the deflection data from the optical measurements, as well as for the control surface angle. The 95% confidence interval for the uncertainty in the local angle of attack measured by the optical measurement system was found to be below 0.01 deg or ±0.2% of typical wing-tip twist deformation. Based on a calibration of the actuator mechanism, the uncertainty of the control surface deflection angle $\boldsymbol{\delta}$ was ±0.05 deg within the same confidence interval. This value includes aeroelastic deformations of the control system mechanism for airspeeds up to 35 m/s. Because the geometric angle of attack linearly depends on both angles according to Eq. (14), the resulting combined uncertainty is found using partial derivatives to be ±0.032 deg. It is likely that measurement errors of this magnitude are small in comparison to the impact of unmodeled physical effects on, for example, control surface efficiencies.

Results

First, some results of reference experiments are compared with numerical simulations. Then, the drag reductions achieved in computations and experiments are documented along with an investigation on the relative merits of flap configurations with different complexity.

Table 3 Coefficients for rigid and flexible wing

Case	α_0, deg	$C_{L,\alpha}$ (1/rad)
Rigid wing exp.	−3.1	5.2
Flex. wing exp.	+0.3	5.9
Rigid wing sim.	−4.7	5.5
Flex. wing sim.	−2.1	6.2

Coefficients and Flap Efficiency

In Table 3, the lift-curve slope and zero-lift angle are listed for both the rigid and the wind-tunnel model with the flexible composite beam. The effect of the flexible structure is to increase both $C_{L,\alpha}$ and α_0. The values for the flexible configuration are for an airspeed of 30 m/s and increase further for larger dynamic pressures. Note that, for the angle of attack range of interest, the flexible wing always produces considerably less lift than the rigid configuration caused by the pitch-down twist of the wing tip.

The numerical model overpredicts the lift-curve slope with approximately 0.3 and computes a somewhat smaller zero-lift angle. Both differences are expected as the boundary layer, which is currently not included in the simulation, has a decambering effect on the wing, leading to an increase of α_0. In this study, the primary interest is in the lift distribution along the span and not the accurate prediction of integral coefficients for low-Reynolds-number flow. Therefore, in the following, simulation results and experimental cases are compared on the basis of lift coefficient, not angle of attack. This is based on the assumption that, for a given total lift, the spanwise lift distribution can still be compared, which requires that boundary-layer thickness distribution does not vary strongly along the span. Considering the very large aspect ratio and minimal sweep angle, the occurrence of significant spanwise flow appears unlikely, and the assumption therefore justified.

Flap efficiencies were determined experimentally by deflecting one control surface at a time and measuring the difference in lift. The applied deflections were in the order of ±5 deg, which was considered to lie within the region of linearity. As expected, the results showed that the leading-edge flaps have only very small effect on lift for the rigid wing. On the flexible configuration, the measured effectiveness of leading-edge flaps increased by 25%, as a result of the pitch-up twist deformation generated by these flaps. Numerically computed efficiencies for the leading-edge flaps agreed well with those measured for the rigid case. However, the simulation model predicted higher than measured leading-edge flap efficiencies $C_{L,\delta}$ on the flexible wing. As the twist deformation caused by flap deflections is computed relatively well, the error is likely related to the smaller than predicted lift response of the wing to this twist deformation. Trailing-edge efficiencies, in comparison, are consistently overpredicted by the simulation, independent of flexibility, which is usually the case for inviscid flow models.[21] For the flow conditions at hand, it is likely that the fairly thick boundary layer reduces the cambering effect of trailing-edge flaps considerably.

For the particular configuration considered here, the direct effect of control surface deflections on the lift distribution is small compared to the importance of twist deformation. Because of the very low torsional stiffness, the aerodynamic moments generated by flap deflections lead to quite significant changes in the spanwise twist distribution. It is above all this mechanism that is exploited to achieve favorable lift distributions. For a more torsionally stiff wing, the aerodynamic efficiency, in particular that of the trailing-edge flaps, would gain much in importance.

Optimization

Numerical optimization is performed for lift coefficients in the range 0.2 to 0.8, and the results are compared with a baseline configuration for which only the angle of attack is changed to obtain the target lift coefficient. Both the baseline and the cases with optimized flap settings were tested in the wind tunnel. To achieve identical lift coefficients, simulations were performed at root incidence angles, which were between 1.6 and 2.4 deg smaller than those run in the wind tunnel.

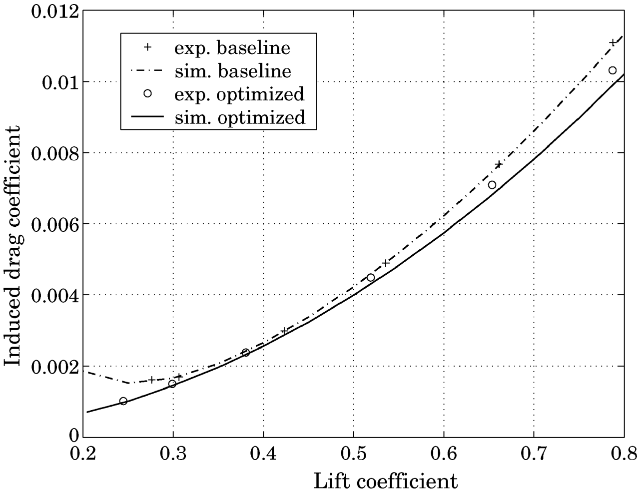

Fig. 6 C_{Di} over C_L for varying dynamic pressure q_∞ with constant wing loading of 150 N/m^2.

Results are presented as diagram of induced drag over lift coefficient. For the case presented in Fig. 6, wing loading remains constant over the C_L range, meaning that the lower C_L values correspond to higher dynamic pressure q_∞. This type of analysis is meant to model operation at different altitudes and speeds for constant aircraft weight.

Especially for relatively low lift coefficients, the experimentally determined induced drag estimations fit very well with the numerical predictions both for the baseline and the optimized flight conditions. For all tested flight conditions, an improvement could be achieved. For high lift coefficients, however, the simulation predicts slightly larger savings than measured.

From the variation of the induced drag for the clean configuration without flap deflections, it can be concluded that there are operating conditions for which the wing in question is already close to optimal. This is representative for an actual aircraft design problem, where an elastic wing would likely be designed with an aerodynamic twist distribution, which yields optimal performance for a certain design point (dynamic pressure and C_L). Nevertheless, significant drag reductions can be achieved at other operating points by employing control surface deflections.

For the aeroelastic configuration considered here, the most significant drag reduction can be obtained at low C_L values and high dynamic pressures, conditions at which low induced drag would be usually expected. The numerical optimization yields a maximum saving of about $\Delta C_{\mathrm{Di}} = 25 \times 10^{-4}$ at $C_L = 0.2$ and 40 m/s. The reason that relatively large gains can be achieved for this condition is the unfavorable lift distribution of the wing without flap deflections. The distribution is characterized by a downward force in the outboard section with large negative twist angles and a slightly larger upward force on the inboard part of the wing. This S-shaped lift distribution generates a considerable amount of induced drag at low C_L values. Even for moderate lift values, the lift distribution is still unfavorable in terms of induced drag, showing an approximately triangular shape, where the outboard 20% of the wing contributes very little to lift. By modifying the spanwise twist distribution using control surface deflections, a lift distribution with much less drag can be reached.

Figure 7 shows the lift distribution in terms of local lift coefficient over the semispan for a specific case with $C_L = 0.2$ and $u_\infty = 30$ m/s. The sharp peaks seen in the computed lift distribution at certain positions result from the geometry of the wind-tunnel model. Because the rigid aerodynamic sections are only attached in points on the internal structural beam, the wing twist angle does not vary smoothly along the span. Discrete jumps in twist angle between the wing segments cause the irregular circulation distribution, which, because of the small magnitude of the peaks, has negligible influence on induced drag. The experimentally obtained distribution does not resolve this small-scale effect. Lift distributions for optimized flap

Table 4 Drag reduction and span efficiency obtained for different flap configurations

n	ΔC_{Di}	e	α, deg
Baseline	0.0	0.256	2.28
3	-17.9×10^{-4}	0.909	3.80
6	-18.2×10^{-4}	0.957	1.26
10	-18.4×10^{-4}	0.979	1.24
20	-18.4×10^{-4}	0.986	1.17

Table 5 Optimal flap settings for the case $C_L = 0.15$ at $u_\infty = 46$ m/s

Sections	1–2	3–4	5–6	7–8	9–10
		Leading edge			
$n = 6$	10.0	10.0	10.0	10.0	10.0
$n = 10$	10.0	10.0	10.0	10.0	9.1
		Trailing edge			
$n = 3$	−3.8	−3.8	−6.3	−6.3	−10.0
$n = 6$	−8.4	−8.4	−7.5	−7.5	−7.7
$n = 10$	−8.8	−8.0	−7.7	−7.4	−8.0

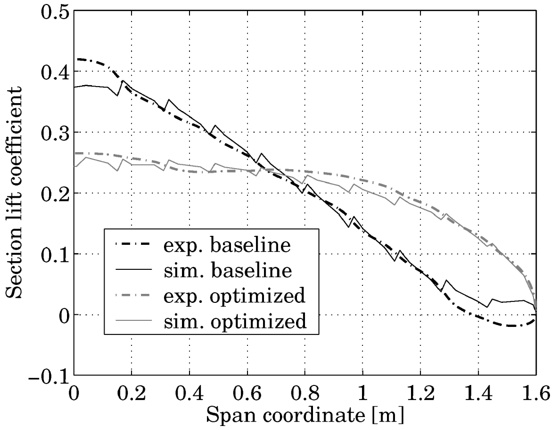

Fig. 7 Spanwise lift distributions.

settings are very close to the elliptic spanwise distribution of circulation, showing the effectiveness of the numerical optimization.

The experimental lift distributions presented in Fig. 7 result from lifting-line analysis using the measured twist angles and control surface settings. Both angles are affected by measurement inaccuracies, as already described, leading to a maximum error of less than ±3% in local lift coefficients.

Flap Configurations

The results shown in Figs. 6 and 7 were obtained for a configuration with 20 individual control surfaces and the angle of attack as design variables. Although such a setup enables a fairly accurate control of the beam deformation and the distribution of camber, it is probably too complex for an aircraft wing. For the more realistic, simplified flap configurations shown in Fig. 4, the achievable drag reductions are slightly smaller.

In Table 4, the possible reduction of induced drag ΔC_{Di} is given along with the corresponding value of Oswald's span efficiency

$$e = C_L^2 \Big/ \pi \Lambda C_{\mathrm{Di}} \tag{16}$$

where Λ is the aspect ratio of the wing. A span efficiency of 1.0 corresponds to the induced drag of the elliptic lift distribution. The listed values were computed for the case with $C_L = 0.15$ at $u_\infty = 46$ m/s, where the possible drag savings are relatively large. Wing-root incidence angles α given in Table 4 refer to values computed by the optimization procedure for the numerical model. Optimal control surface deflections for this particular case are listed in Table 5.

Table 4 suggests that three trailing-edge control surfaces alone are sufficient to achieve a significant reduction in induced drag. However, this is only true in connection with the corresponding wing-root incidence angle of 3.8 deg, which is one of the design variables. By using leading-edge flaps, slightly better induced drag reductions can be obtained without the need of an increased root incidence angle. This might be relevant for configurations where a reduced range of operating angles of attack entails advantages in parasitic drag.

The advantage of using leading-edge flaps for torsionally flexible wings lies in their ability to generate considerable pitch-up twist moment and a small positive aerodynamic lift increment. Naturally, trailing-edge surfaces are much more efficient in generating additional lift; however, at the same time, they always produce a pitch-down twist moment, causing a deformation of the complete wing counteracting the lift increment. Therefore, leading-edge flaps can be more effectively used to control wing twist deformation.

Drag-reduction efforts in aircraft design will always aim at reducing total drag of the complete trimmed configuration, which can depend in a complex manner on angle of attack and flap deflections. The potential benefits of leading-edge flaps just described must hence also be judged by the effect they most likely have on viscous drag components.

Computational Aspects

When formulating the drag-minimization problem as a linear least-squares problem according to Eqs. (9) and (10), the computational cost is moderate. For six design variables, a single solution to the optimization problem is computed in about 15 min on a desktop computer with 1.4-GHz Athlon processor. Using pressure integration and nonlinear programming, mesh requirements and the large number of finite difference gradient calculations lead to at least 10-fold increased computational effort. With mesh resolutions sufficient for accuracy, computation times become unacceptable.

Conclusions

The investigation demonstrated that the induced drag of an elastic wing configuration can be reduced significantly by means of conventional leading- and trailing-edge control surfaces. The use of leading-edge control surfaces can be beneficial if the optimal twist distribution requires that large sectional pitch moments are generated. Furthermore, the use of more than six control surfaces does not appear to pay off, unless the marginal additional savings really compensate for the increased cost and complexity. If savings of relevant magnitude are possible in the first place depends primarily on the quality of the lift distribution and the flexibility of the wing. Relatively rigid wings will show less variability of their spanwise loading under different flight conditions, while highly flexible ones will likely operate with very unfavorable lift distributions in parts of the flight envelope. These are the configurations where substantial drag reductions can be achieved by means of control surfaces.

The use of potential flow methods for a induced drag-reduction problem at Reynolds numbers below 10^6 is possible, but difficult. Boundary-layer effects have a significant impact on chordwise pressure distribution and control surface efficiencies, so that potential flow results might be hard to interpret when experimental comparisons are not available. The inclusion of a boundary-layer model in the numerical method is expected to improve the prediction of control surface efficiencies in particular.

Acknowledgments

Construction of the wind-tunnel model, definition of the structural analysis model, as well as current and upcoming experimental activities, are financed by the European Union under the Fifth Research Framework, through the project Active Aeroelastic Aircraft Structures, Project Number GRD-1-2001-40122. The first author's work, comprising aerodynamic modeling, optimization, and computational studies, are financed by the Swedish National Program for Aeronautics Research.

References

[1] Stanewsky, E., "Adaptive Wing and Flow Control Technology," *Progress in Aerospace Sciences*, Vol. 37, No. 7, 2001, pp. 583–667.

[2] Goraj, Z., Frydrychiewicz, A., and Winiecki, J., "Design Concept of a High-Altitude Long-Endurance Unmanned Aerial Vehicle," *Aircraft Design*, Vol. 2, No. 1, 1999, pp. 19–44.

[3] Thornton, S. V., "Reduction of Structural Loads Using Maneuver Load Control on the Advanced Fighter Technology Integration (AFTI) Mission Adaptive Wing," NASA TM-4526, Sept. 1993.

[4] Simpson, J., Schweiger, J., and Kuzmina, S., "Design of an Adaptive Wing Shape Control Concept for Minimum Induced Drag of a Transport Aircraft," *CEAS/AIAA/NvVL International Forum for Aeroelasticity and Structural Dynamics*, Paper GE-11, Netherlands Association of Aeronautical Engineers (NVvL), Amsterdam, June 2003.

[5] Zink, P. S., Mavris, D. N., and Raveh, D. E., "Maneuver Trim Optimization Techniques for Active Aeroelastic Wings," *Journal of Aircraft*, Vol. 38, No. 6, 2001, pp. 1139–1146.

[6] Dowell, E. H., Bliss, D. B., and Clark, R. L., "Aeroelastic Wing with Leading- and Trailing-Edge Control Surfaces," *Journal of Aircraft*, Vol. 40, No. 3, 2003, pp. 559–565.

[7] Pendleton, E., Bessette, D., Field, P., Miller, G., and Griffin, K., "The Active Aeroelastic Wing Flight Research Program: Technical Program and Model Analytical Development," *Journal of Aircraft*, Vol. 37, No. 4, 2000, pp. 554–561.

[8] Kuzmina, S., Ishmuratov, F., Kuzmin, V., and Sviridenko, Y., "Estimation of Flying Vehicle Induced Drag Changing due to Deformation of Lifting Surfaces," *CEAS/AIAA/NvVL International Forum for Aeroelasticity and Structural Dynamics*, Paper RU-2, Netherlands Association of Aeronautical Engineers (NVvL), Amsterdam, June 2003.

[9] Althaus, D., *Niedriggeschwindigkeitsprofile*, Vieweg Verlag, Braunschweig, 1996, pp. 232–329.

[10] Schweiger, J., and Suleman, A., "The European Research Project 'Active Aeroelastic Aircraft Structures'," *CEAS/AIAA/NvVL International Forum for Aeroelasticity and Structural Dynamics*, Paper GE-10, Netherlands Association of Aeronautical Engineers (NVvL), Amsterdam, June 2003.

[11] Eller, D., and Carlsson, M., "An Efficient Aerodynamic Boundary Element Method and Its Experimental Validation," *Aerospace Science and Technology*, Vol. 7, No. 7, 2003, pp. 532–539.

[12] Katz, J., and Plotkin, A., *Low Speed Aerodynamics*, 2nd ed., Cambridge Univ. Press, Cambridge, England, U.K., 2001, Chap. 12.

[13] Hackbusch, W., and Nowak, Z. P., "On the Fast Matrix Multiplication in the Boundary Element Method by Panel Clustering," *Numerische Mathematik*, Vol. 54, No. 4, 1989, pp. 463–491.

[14] Albano, E., and Rodden, W. P., "A Doublet-Lattice Method for Calculating the Lift Distribution on Oscillating Surfaces in Subsonic Flow," *AIAA Journal*, Vol. 2, No. 7, 1969, pp. 279–285.

[15] Eppler, R., *Airfoil Design and Data*, Springer-Verlag, Berlin, 1990, Chap. 5.

[16] *Nastran Reference Manual*, MSC.Nastran 2004, MSC Software Corp., Los Angeles, CA, 2004.

[17] *Optimization Toolbox: User's Guide*, Matlab 6.1, The Math Works, Inc., Natick, MA, 2001.

[18] *ProReflex, Technical Reference*, Qualisys AB, Sävedalen, Sweden, 1997.

[19] Kuttenkeuler, J., and Carlsson, M., "Optical Deformation Measurements in Wind Tunnel Testing," *International Forum on Aeroelasticity and Structural Dynamics*, Vol. III, Associacion de Ingenieros Aeronauticos de España, Madrid, 2001, pp. 499–508.

[20] Barlow, J. B., Rae, W. H., and Pope, A., *Low-Speed Wind Tunnel Testing*, 3rd ed., Wiley, New York, 1999, Chap. 8.

[21] Schlichting, H., and Truckenbrodt, E., *Aerodynamik des Flugzeuges*, Springer-Verlag, Berlin, 1959.

[22] Multhopp, H., "Die Berechnung der Auftriebsverteilung von Tragflügeln," *Luftfahrtforschung*, Vol. 15, No. 14, 1938, pp. 153–169.